Chemical Geology 345 (2013) 99–112

Contents lists available at SciVerse ScienceDirect

Chemical Geology

journal homepage: www.elsevier.com/locate/chemgeo

Laser-ablation split-stream ICP petrochronology

Andrew R.C. Kylander-Clark *, Bradley R. Hacker, John M. Cottle

Department of Earth Science, University of California, Santa Barbara, CA 93106, United States

ARTICLE INFO

Article history:
Received 22 August 2012
Received in revised form 21 February 2013
Accepted 21 February 2013
Available online 1 March 2013

Editor: K. Mezger

Keywords:
Laser ablation
Geochronology
Geochemistry
Accessory minerals

ABSTRACT

Laser-ablation split-stream (LASS) analysis—high-speed, high spatial-resolution, simultaneous isotopic and elemental analysis—enables petrochronology at a new level, through the interpretation of isotopic dates combined with elemental abundances and/or isotopic tracers. This contribution begins with an introduction to petrochronology, presents a new LASS technique using dual multi-collector–single-collector inductively-coupled plasma mass spectrometry, and offers examples of how this technique is used to decipher the evolution of rocks with complex geologic histories.

1. Introduction

Petrochronology is the interpretation of isotopic dates in the light of complementary elemental or isotopic information from the same mineral(s). It is a relatively new science whose nascent stages might be said to have begun with the use of U/Th to differentiate between igneous and metamorphic zircons (Ahrens et al., 1967) or the use of Y to identify monazite that coexisted with garnet or xenotime (Pyle and Spear, 1999). As outlined below, the field is expanding rapidly to exploit in situ trace elements and Hf isotopes in zircon; trace elements and Nd isotopes in monazite; trace elements, Sm–Nd and Sr isotopes in titanite; and trace elements and Hf isotopes in rutile—to name but a few. All of these approaches are founded on the same principle: that the combination of isotopic dates and elemental/isotopic tracers enables a powerful synergy that transforms our ability to address Earth Science questions.

There are half a dozen principal components to petrochronology that can be used to varying degrees of success in different minerals. The texture of a mineral—assessed through optical microscopy and back-scattered electron (BSE) imaging—can help identify the reactions that formed, recrystallized, or partially consumed the mineral or identify the deformation or fluid flow coincident with such. The qualitative zoning of a mineral—assessed through cathodoluminescence (CL), BSE imaging or X-ray mapping—can assist in matching mineral (re)crystallization to specific igneous, metamorphic or deformation events, or the presence or absence of other minerals. The volume proportion of an accessory phase can be used as a qualitative barometer or thermometer in favorable circumstances when accompanied by pseudosection construction. The presence or absence of inclusions can be a guide to minerals that were present or absent at the time the host phase grew, as can the concentrations of certain trace elements (e.g., Y and Eu/Eu*). The concentrations of other trace elements (e.g., Ti, Zr, and Y)—measured by electron probe microanalysis (EPMA) or ICP—can be used in quantitative thermobarometry to establish pressures and/or temperatures. Finally, complementary isotopes (e.g., Hf, Sm–Nd or Sr) can be used to extract information such as magma source and mixing characteristics, further age information, the fluxes and sources of fluids, and provenance.

The most widely employed minerals for petrochronology are zircon, monazite, titanite and rutile. These four accessory phases are found in a broad range of bulk-rock compositions and can persist through multiple sedimentary transport, metamorphic, and igneous events that span a wide range of pressures, temperatures, and deformation and fluid conditions. They often grow in response to changes in these parameters and may record these changes in distinct compositional domains that can be related to mineral-forming reactions and dated (Giere and Sorensen, 2004; Dumond et al., 2006; Cottle et al., 2009c). Each readily accepts U and/or Th into its structure, providing two or three independent decay schemes—$^{238}U \rightarrow {}^{206}Pb$, $^{235}U \rightarrow {}^{207}Pb$ and $^{232}Th \rightarrow {}^{208}Pb$—that can be used to assess closed system behavior. For nearly all zircon and monazite—and many titanite and rutile—the U or Th concentrations are sufficient to permit measurement of precise isotopic dates at the tens-of-micron scale. The parents of these decay chains are effectively immobile, and the final product of each of these schemes—Pb—has sufficiently low diffusivities over geologic time (Cherniak and Watson, 2003; Cherniak et al., 2004) to allow age information from multiple episodes of growth, dissolution and re-precipitation to be preserved within single crystals. Below we *summarize* the roles for two of these four minerals—

* Corresponding author. Tel.: +1 805 893 7097.
E-mail address: kylander@geol.ucsb.edu (A.R.C. Kylander-Clark).

0009-2541/$ – see front matter © 2013 Published by Elsevier B.V.
http://dx.doi.org/10.1016/j.chemgeo.2013.02.019

zircon and monazite—as petrochronometers, focusing in particular on the aspects that are accessible through laser-ablation split-stream (LASS) analysis.

1.1. Zircon petrochronology

Zircon has been the quintessential geochronometer for many years because it is common, contains the twin U decay schemes and has relatively little common Pb. It crystallizes in silica-saturated to intermediate-composition igneous rocks, and is present in a broad range of metamorphic rocks because Zr and/or Si are liberated by a variety of metamorphic reactions (Fraser et al., 1997; Bingen et al., 2001; Degeling et al., 2001; Young et al., 2007). Some zircon-forming reactions—such as the formation of zircon during the pressure-induced transformation of ilmenite to rutile (Bingen et al., 2001; Root et al., 2004) or the decompression-induced breakdown of garnet to zircon (Degeling et al., 2001)—have petrologic significance, allowing the zircon date to be tied to specific, petrologically meaningful reactions. Deformation of zircon may lead to compositional re-equilibration, providing an opportunity for dating deformation (Timms et al., 2010). Inclusions in zircon can also provide spectacular constraints on the PT conditions at which particular parts of a zircon (re)crystallized, enabling tight control on the time and duration of the PT path (Hermann et al., 2001; Katayama et al., 2002; Liu et al., 2006). CL images of zircons (Nasdala et al., 2003) are also helpful in assessing whether parts of grains are igneous (typified by oscillatory or sector zoning) or metamorphic (typified by patchy, fir-tree, transgressive, or no zoning), and in decoding zircon history (Vavra, 1990; Hanchar and Rudnick, 1995; Rubatto et al., 2000; Corfu et al., 2003).

Zircon has a tetrahedral Si site and a distorted octahedral Zr site (Finch and Hanchar, 2003). The main impurity in zircon, Hf (up to 22 wt.%, Uher and Černý, 1998) enters the Zr site, as do the other main quadrivalent impurities Th, U, and Ti (Frondel, 1953). The rare-earth elements (REE), Y and Sc enter the Zr site in a coupled substitution principally with pentavalent Nb, Ta or P (Eskova, 1959; Speer, 1982; Hanchar et al., 2001). If partitioning among competing phases was well understood and quantified with activity models, each of these trace elements could, in principle, be used to gain quantitative petrochronologic insight. Presently, however, trace-element abundances in zircons are used as qualitative petrologic indicators in four principal ways. 1) The differences in the solubilities of Th and U in fluids and zircon mean that the Th/U ratio is a qualitative indicator of whether zircon is igneous or metamorphic (Ahrens, 1965; Hoskin and Ireland, 2000; Hokada and Harley, 2004; but see Konzett et al., 1998; Möller et al., 2002; Rubatto et al., 2009). 2) The Ti solubility in zircon in the presence of quartz and a Ti-saturating phase can be used as a quantitative thermometer (Watson and Harrison, 2005; Watson et al., 2006; Ferry and Watson, 2007). 3) The HREE are closer in size than the LREE to Zr, and therefore are incorporated preferentially into zircon. Because garnet and xenotime also incorporate HREE, however, the slope of the normalized HREE abundances can be used to assess whether zircon (re)crystallized when garnet and/or xenotime were present or absent (Rubatto et al., 1999; Hoskin and Ireland, 2000; Rubatto, 2002; Hermann and Rubatto, 2003; Hoskin and Schaltegger, 2003; Root et al., 2004; McClelland et al., 2009; Rubatto et al., 2009). 4) The presence/absence of a negative Eu anomaly, Eu/Eu*, can be used to assess whether feldspar (plagioclase more so than K-feldspar, Nagasawa, 1971; Gromet and Silver, 1983) was present/absent during the (re)crystallization of zircon (Hinton and Upton, 1991; Schaltegger et al., 1999; Hoskin and Ireland, 2000; Belousova et al., 2002; Rubatto, 2002).

1.2. Monazite petrochronology

Monazite has recently begun to take a leading role in petrochronology because it has not only all the advantages of zircon—twin U decay schemes, little common Pb, and a high closure temperature—but it also hosts the $^{232}Th \rightarrow {}^{208}Pb$ decay scheme, and can be more easily tied to petrology because of its ability to take up a broad range of trace elements (e.g., Foster et al., 2002; Kohn and Malloy, 2004; Kohn et al., 2005; Cottle et al., 2009a, 2009b; Janots et al., 2009).

As many as five texturally distinct generations of monazite have been identified in single samples (Kohn et al., 2005), and the high closure temperature for monazite (>900 °C for 10 μm grains cooled at 10 K/Myr, Gerdes et al., 2007; Cherniak and Pyle, 2008) means that complicated histories can be preserved (Harrison et al., 1995). Monazite with specific microstructures can be used to date deformation (Williams et al., 2002; Dahl et al., 2005). In addition, monazite participates in a large number of reactions (Catlos et al., 2002; Pyle and Spear, 2003; Spear and Pyle, 2010) and can host a wide variety of inclusions; both of these features can enable it to be tied closely to the petrological evolution of a rock (Smith and Barreiro, 1990; Simpson et al., 2000; Janots et al., 2008; Kelsey et al., 2008; Spear and Pyle, 2010). Numerous studies have exploited the proclivity of monazite to be included in garnet to date garnet growth (Bell and Welch, 2002), and monazite shielded within garnet can even preserve Pb at temperatures in excess of 1000 °C (Hacker et al., 2000; Hoisch et al., 2008).

Monazite has a 9-fold coordinated REE site and a tetrahedral P site (Burt, 1989; Ni et al., 1995) that take up a wide range of trace elements. Zoning can be used to assess whether a monazite is igneous or metamorphic and to unravel (re)crystallization histories (DeWolf et al., 1993; Montel, 1993; Hawkins and Bowring, 1997; Zhu et al., 1997; Ayers et al., 1999). Th and U enter the monazite REE site through coupled substitution with Ca into the same site or through coupled substitution with Si into the P site (Gramaccioli and Segalstad, 1978; Mohr, 1984; Chaudhuri and Newesely, 1993; Franz et al., 1996; Poitrasson et al., 1996; Ventura et al., 1996; Zhu and O'Nions, 1999a; Williams et al., 2007); their strong partitioning into monazite means that Th and U may show Rayleigh fractionation behavior, which can be exploited to reveal relative growth histories (Wark and Miller, 1993; Bea et al., 1998). Zoning in Y, Ca, Si, Sr, Ba, REE, U and Th, enables monazite (re)crystallization to be tied to particular metamorphic reactions (e.g., Bingen and van Breemen, 1998; Kohn and Malloy, 2004; Corrie and Kohn, 2008), including melting (Wolf and London, 1995), which can then be dated to gain a more complete understanding of tectonic processes (Terry et al., 2000; Wing et al., 2003; Goncalves et al., 2005; Pyle et al., 2005; Yang et al., 2006; Spear et al., 2008). The presence or absence of feldspar during monazite (re)crystallization can be monitored using Eu/Eu* (Zhu and O'Nions, 1999b; Hermann and Rubatto, 2003; Rubatto et al., 2006) or Sr (Finger and Krenn, 2007). Yttrium is the trace element most exploited for petrologic purposes. The exchange of Y between garnet and monazite is a quantitative thermometer (Pyle et al., 2001; Berger et al., 2005; Pyle and Baldwin, 2006), but perhaps more importantly, garnet—and, of course, xenotime—are major sinks for Y + HREE and exert a strong control over the Y + HREE content of monazite (e.g., Pyle and Spear, 1999; Zhu and O'Nions, 1999a; Foster et al., 2000; Pyle et al., 2001; Foster et al., 2002; Pyle and Spear, 2003; Foster et al., 2004; Gibson et al., 2004; Kohn et al., 2005; McFarlane et al., 2005; Kelly et al., 2006; Rubatto et al., 2006; Tomkins and Pattison, 2007). Monazite growth that occurs during garnet or xenotime breakdown will be enriched in Y + HREE. Conversely, monazite growth concomitant with garnet or xenotime growth will be depleted in Y + HREE. The record of growth and breakdown episodes should, at least in part, be reflected in the Y zonation within a monazite. It is therefore possible to combine the information on Y + HREE content in monazite with bulk-rock textural and microstructural observations and geochronological analyses to reconstruct a detailed P–T–t–D path for garnet- and monazite-bearing rocks.

2. Existing petrochronology techniques

Petrochronology studies have mostly been conducted by using LA-ICPMS or secondary ion mass spectrometry (SIMS) to measure

dates in one analytical session and using electron-probe microanalysis (EPMA), LA-ICPMS or SIMS to measure elemental composition in a second analytical session (e.g., Rubatto, 2002). While powerful, these techniques have two disadvantages: 1) the area required for spot analyses must be big enough for two adjacent spots or the material must be repolished between analyses, and 2) the isotopic and elemental information are extracted from different volumes of material. More recently developed techniques use simultaneous measurement of elements and dates by either quadrupole (Q) ICP-MS (e.g., Li et al., 2000) single-collector (SC), magnetic-sector ICP-MS (e.g., Kohn and Corrie, 2011), or SIMS (e.g., McClelland et al., 2009). These approaches allow measurement of multiple isotopes of interest during a single spot analysis. The advantage of these approaches is the ability to directly link a date to element abundance for the same volume of material, but there are disadvantages of either reduced precision (by design, Q- and SC-ICPMS have lower sensitivity and shorter counting times compared to a multi-collector (MC) ICP-MS) or long counting times (SIMS analyses require ~15 min per analysis for U–Pb + trace elements).

The laser-ablation split-stream or LASS technique was thus introduced to take advantage of both types of ICP: the MC-ICPMS, with its superior isotopic ratio measurement capabilities (e.g., for U–Th–Pb and Hf), and the SC-ICPMS, capable of rapid measurement over a large mass range (e.g., for element abundance analysis). LASS was first described by Yuan et al. (2008), and subsequently adopted by Xie et al. (2008) and Chen et al. (2010). These researchers split the laser aerosol stream, directing part of it to an MC-ICPMS to measure the Hf isotopic ratio, and the rest to a Q-ICPMS to measure U–Pb ages and trace-element abundances. Here we describe an analytical setup in which the aerosol stream is split between an MC-ICPMS to measure U–Th–Pb isotopic ratios and a SC-ICPMS to measure elemental abundances. This approach significantly improves the precision of the date from each spot analysis and also greatly reduces the volume of ablated material compared with the method introduced by Yuan et al. (2008).

Table 1
Instrumental parameters of laser-ablation split-stream ICP-MS.

	MC-ICP-MS	SC-ICP-MS
Instrument model	Nu plasma HR	Nu AttoM
RF forward power	1300 W	1300 W
RF reflected power	<10 W	<10 W
Coolant gas	13 L/min	13 L/min
Auxiliary gas	0.8 L/min	0.8 L/min
Make up gas	~1.9 L/min — flow to AttoM	~1.9 L/min — flow to plasma
Monitored masses (E-Scan — zircon example)	^{238}U, ^{232}Th, ^{208}Pb, ^{207}Pb, ^{206}Pb, ^{204}Pb/^{204}Hg	^{139}La, ^{140}Ce, ^{141}Pr, ^{146}Nd, ^{147}Sm, ^{153}Eu, ^{157}Gd, ^{159} Tb, ^{163}Dy, ^{165}Ho, ^{166}Er, ^{169}Tm, ^{172}Yb, ^{176}Lu, ^{179}Hf
Monitored masses (linked scan — monazite example)	^{238}U, ^{232}Th, ^{208}Pb, ^{207}Pb, ^{206}Pb, ^{204}Pb/^{204}Hg	^{31}P, ^{44}Ca, ^{88}Sr, ^{89}Y, ^{139}La, ^{140}Ce, ^{141}Pr, ^{146}Nd, ^{147}Sm, ^{153}Eu, ^{157}Gd, ^{163}Dy, ^{166}Er, ^{172}Yb, ^{180}Hf
^{238}U sensitivity, dry solution	0.7% (290 V/ng)	0.2% (80 V/ng)
throughput on LASS	0.3% (140 V/ng) ^{238}U	(38 V/ng) ^{179}Hf
Dwell time	200 ms	E-Scan: 0.3 ms linked scan: 200 ms
Integration	0.2 s	E-Scan: 0.5 s linked scan: 2 s
		Laser-ablation system
Instrument model		Photon Machines Analyte 193
Laser		ATLEX-SI 193 nm ArF excimer
Fluence		3.5 J/cm^2
Repetition rate		3–4 Hz
Excavation rate		~0.07 μm/pulse
Delay between analyses		20 s
Ablation duration		~30 s
Carrier gas (He) flow		0.25 L/min

3. Laser-ablation split-stream instrumentation and techniques

The LASS lab at the University of California, Santa Barbara houses two ICP-MS instruments—a Nu *Plasma HR* MC-ICPMS and a Nu *AttoM* SC-ICPMS (Nu Instruments Ltd., Wrexham, UK)—and an *Analyte 193* ArF laser-ablation system (Photon Machines, San Diego, USA; Fig. 1; Table 1). The Analyte 193 is based on an ATLEX SI ArF 193 nm wavelength excimer laser and equipped with a low-volume HeLex sample cell modified from the design of Eggins et al. (1998, 2005). The cell enables rapid washout times, with 99% reduction in signal intensity in <1.5 s. The output energy of the laser is fixed at 3–7 mJ and attenuated before reaching the sample cell. The laser fluence, calculated from periodic measurements at the sample surface with a Gentec-EO power meter, is 3–4 J/cm^2, and produces an ablation rate of 0.05–0.1 μm/pulse. The spot size used depends on the petrochronometer, but is typically 10 μm for monazite and 20–30 μm for zircon.

The laser aerosol is carried by He from the sample cell to a mixing bulb in which the sample + He is mixed with Ar to stabilize the aerosol input to the plasma. Boiled liquid argon and ultrahigh-purity He are used, and passed through activated charcoal and gold-coated quartz filters upstream of the mass-flow controllers. The He–Ar aerosol is immediately split upon exiting the mixing bulb, with approximately half the ablation stream directed to each ICPMS. The ^{204}Hg background on the Plasma is typically ~500 counts per second (cps) and introduced primarily by the He; the total Pb background is <1000 cps.

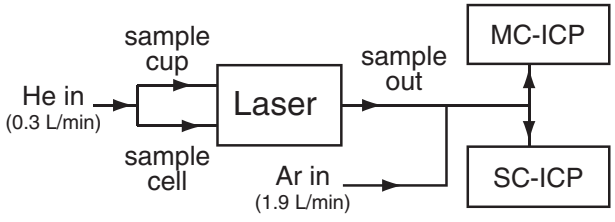

Fig. 1. Instrumentation setup for laser-ablation split-stream (LASS) petrochronology.

Trace element- and/or U–Th–Pb isotope abundances are measured on the AttoM SC-ICPMS in one of two modes: E-Scan mode or linked-scan mode. The AttoM is a Nier–Johnson geometry instrument with a single, discrete-dynode electron multiplier. Signal sizes varying by six orders of magnitude can be measured, and an additional three orders of magnitude larger signal can be measured using a customized deflection system.

In E-Scan mode, the magnet is set to a fixed position and the post-electrostatic analyzer (ESA) deflector voltages are altered to change the mass seen by the detector. The deflector voltages can be altered every 10 μs, and allowing for settling (typically set to 30 μs), a minimum dwell time/isotope is typically 130 μs. The total acquisition time for 1 sweep of the masses of interest is generally kept to ca. 2.5–4 ms to minimize short-term measurement uncertainty associated with plasma flicker. This mode allows the measurement of isotopes within a 40% mass range, enabling the measurement of, for example, La–Hf, or Nd–Hf + U–Th–Pb. Because matrix-matched reference materials are used to bracket samples, a simple linear correction (i.e., no internal correction) is used for unknowns. REE concentrations calculated by this method are comparable to those calculated with an internal standard correction (Fig. 2, Liu et al., 2010a).

Linked-scan mode on the AttoM is used to make measurements over the entire mass range, but, as a result, precision is lower than E-Scan mode. Measurements are collected during a controlled 220 ms magnet sweep (100 ms each direction + 20 ms settle time). To maximize

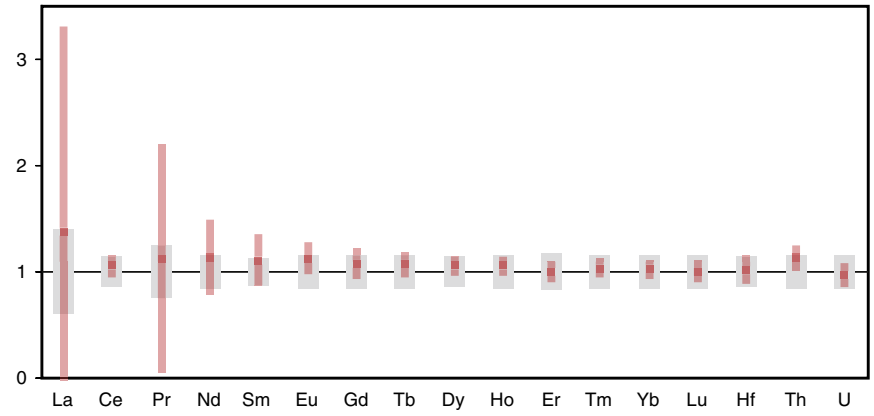

Fig. 2. REE concentrations of the GJ1 zircon calculated using 91500 as the reference standard. Data in this study (orange) is shown as a deviation from concentrations obtained by Liu et al. (2010). Error bars show the standard deviation of each set of data. Values calculated within this study are equivalent to those of Liu et al. (2010). (For interpretation of the references to color in this figure legend, the reader is referred to the web version of this article.)

counting time, each isotope of interest is deflected into the ion counter by simultaneous use of the magnet and the post-ESA deflectors. As the magnet sweeps, each mass remains in the ion counter for up to 40% of its mass along the magnet sweep. Thus, the measurement precision on isotopes similar in mass is reduced because the deflectors must switch to the next isotope earlier. For example, when measuring REEs and Hf, time spent on ^{180}Hf is much greater than that spent on ^{140}Ce, because ^{140}Ce lies between other isotopes of interest (i.e., ^{139}La and ^{141}Pr). Thus, to improve the measurement precision, only elements of specific petrologic significance are chosen. The linked-scan mode is primarily used for monazite, in which a larger mass range is required to scan all petrologically relevant elements.

Elemental abundances and their uncertainties are calculated by interleaving matrix-matched reference materials among samples and then reducing the collected data using the Iolite software (Woodhead et al., 2007; Paton et al., 2010). Using E-Scan mode, a typical ablated volume (~20 ng; e.g., 24 × 10 μm spot on zircon) generally yields a 2SE precision of 2–5% for elements more abundant than 100 ppm, 5–10% for elements down to 1 ppm, and >10% for those less than 1 ppm. Using the linked-scan mode for 1–3 ng of monazite (e.g., 8 × 5 μm spot) yields 10–20% uncertainty for elements more abundant than 100 ppm, and up to 50% for elements between 5 and 100 ppm (Fig. 3). Typical uncertainties associated with single LASS U–Th–Pb (E-Scan) measurements on the AttoM for ~130 ng (e.g., 50 × 15 μm spot on zircon) of material are ≤2% for ^{238}U/^{206}Pb age and depend strongly on age and U or Th content for ^{207}Pb/^{206}Pb and ^{232}Th/^{208}Pb ages, respectively (typically 3–10%). If U–Th–Pb + REEs (E-Scan) are measured, age precision drops considerably (Fig. 4; typical range of 5–10%, for all systems of interest).

The UCSB Nu Plasma is equipped with a fixed collector array of 12 Faraday cups and four low-mass ion counters. During analytical sessions in which U–Th–Pb is measured on the Nu Plasma (most cases except, for example, Hf isotopes on zircon, or Nd isotopes on monazite) ^{238}U and ^{232}Th are measured on Faraday cups equipped with 10^{11} ohm resistors, and ^{208}Pb, ^{207}Pb, ^{206}Pb and ^{204}Pb + Hg isotopes are typically measured on four ETP discrete-dynode electron multipliers, but other configurations are possible—i.e., ^{208}Pb, ^{207}Pb and ^{206}Pb on Faraday cups and ^{204}Pb + Hg and ^{202}Hg on ion counters (Table 2). U–Th–Pb isotopic ratios and their uncertainties are calculated using iolite (Paton et al., 2010). Precision on individual analyses varies by volume and U, Th, and Pb concentrations. For zircon, a typical ablation of 12–26 ng of material yields 1–1.5% for ^{206}Pb/^{238}U ratios and 0.3–1% on ^{207}Pb/^{206}Pb ratios (2SE, using down-hole elemental-fractionation correction; Paton et al., 2010; Fig. 5, Table DR1). Monazite yields ^{208}Pb/^{232}Th, ^{206}Pb/^{238}U, and ^{207}Pb/^{206}Pb ratios with 0.5–2.5%, 0.6–1.5%, and 0.3–1.5% precision (2SE), respectively for ~1–3 ng of ablated material (Fig. 6; Table DR2). Throughout the experiments run during this study, the general absence of measurable 204 in zircon and monazite in our collection of standards and unknowns meant that there was no need for a common Pb correction, i.e., the relatively small uncertainty in age due to common Pb contents is incorporated in the external reproducibility of the secondary reference materials.

The Nu Plasma can also be used to accurately and precisely measure Hf (in zircon) or Nd (in monazite) while U–Th–Pb ± REEs are measured on the AttoM. The 10 central Faraday cups measure ^{180}Hf to ^{171}Yb (Table 2). As described above, the AttoM is used to simultaneously measure a date (U–Th–Pb only) or REEs + date (Nd–U) in E-Scan mode.

4. LASS data from standard reference materials

4.1. Zircon

To demonstrate the efficacy of the LASS approach, here we report analyses of multiple zircon reference materials (RMs) measured over a one-year period (2011): 91500 (Wiedenbeck et al., 1995), GJ1

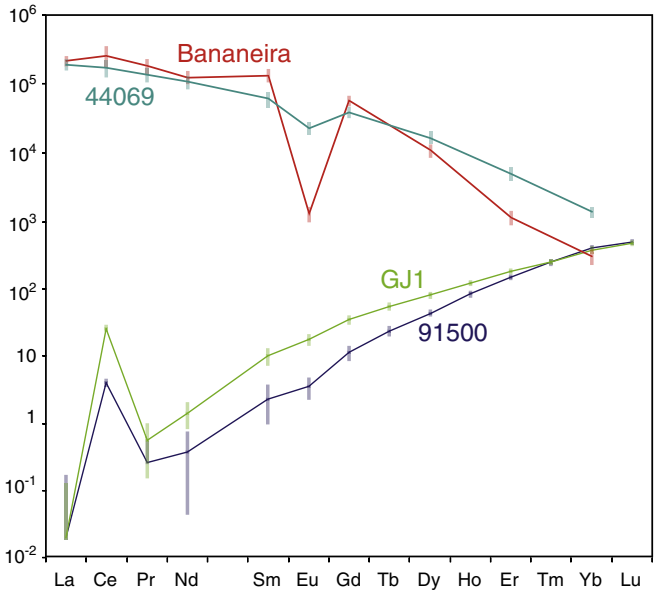

Fig. 3. Chondrite-normalized concentrations (and errors) of REE in reference materials using the AttoM in the LASS configuration. Monazite reference materials 44069 and Bananeira were analyzed from ~2 ng of material in linked-scan mode. Zircon reference materials GJ1 and 91500 were obtained from ~25 ng of material in E-Scan mode.

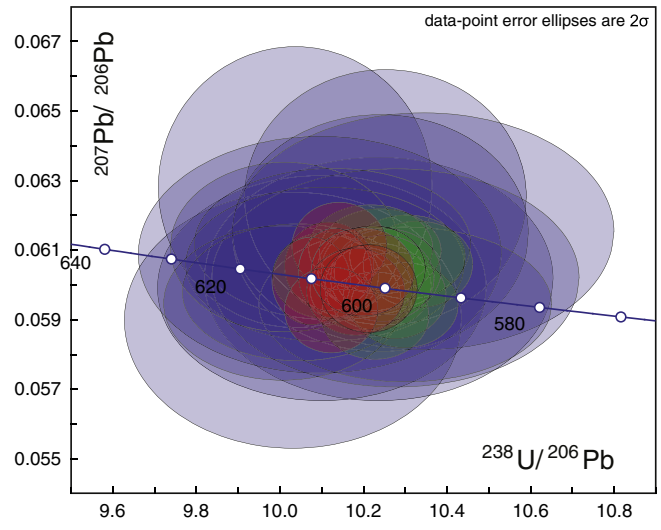

Fig. 4. Comparison between secondary-standard analyses of the reference material GJ1 between LASS (red; U–Pb + REE + Hf), LA-MC-ICPMS (green; U–Pb only), and LA-SC-ICPMS in E-Scan mode (blue; U–Pb + REE + Hf) during a 3 separate analytical sessions (uncertainties are propagated to include the variability in the primary RM analyses). Spot size and depth of the different analysis types are comparable (~24 × 8 μm). Because of natural variability of the primary-RM analyses (91500)—due to drift in mass bias, matrix effects, heterogeneity, etc.—the uncertainties of LASS and LA-MC-ICPMS analyses are similar. The increased counting time and sensitivity of a MC-ICPMS vs. a SC-ICPMS easily outweighs the decrease in ablated material seen by the MC during a LASS analysis. (For interpretation of the references to color in this figure legend, the reader is referred to the web version of this article.)

(Jackson et al., 2004), Plešovice (Slama et al., 2008), SL1 (Gehrels, 2000), Peixe (Dickinson and Gehrels, 2003), Seiland (Pedersen et al., 1989), FC-1 (Paces and Miller, 1993) and R33 (Black et al., 2004). The majority of data reported are from reference materials 91500, GJ1, and Plešovice; these were used as the primary and secondary standards within most analytical sessions. The 91500 RM was used as the primary standard for both U–Th–Pb and REE concentrations for consistency; all other RMs were treated as unknowns, and therefore demonstrate the accuracy of the LASS results. U–Pb, trace-element, and Hf data are presented in Tables DR1, DR3, and DR4, and Figs. 5 and 7.

4.1.1. U–Th–Pb (MC-ICP) + trace-element (SC-ICP) data

The 91500 zircon (81 ppm U, 29 ppm Th, 15 ppm Pb, 1062.4 ± 0.4 Ma) yielded a long-term weighted mean $^{206}Pb/^{238}U$ age of 1062.4 ± 0.5 (0.06% 2SE, MSWD = 0.6) from 286 analyses. The uncertainty on an individual $^{206}Pb/^{238}U$ measurement depends on the volume of ablated material—typically a 24 μm diameter and 8 μm deep cylinder—but was chiefly 1–1.5%. The uncertainty on an individual $^{207}Pb/^{206}Pb$ ratio was typically <1%, however, the long-term reproducibility is 1.5%, yielding a $^{207}Pb/^{206}Pb$ ratio of 0.074826 ± 0.000056 (0.07% 2SE, MSWD = 1.0). We attribute this 1.5% variation to shot-to-shot variation in laser energy—which we know from meter measurement varies by 3%—or cell flow dynamics, or both.

The precision of REE element patterns for 91500 depends on spot size, ablation rate, abundance, etc., as stated in Section 4. REE and Hf intensities commonly covary among the RMs (e.g., when the intensity of the Hf signal for 91500 increases during a run, it also increases for GJ-1 and Plešovice at the same time), allowing for correction of instrument drift.

The specific piece of the GJ-1 zircon RM (Jackson et al., 2004) used for this study was analyzed by NIGL (D. Condon, personal comm.) to have a $^{206}Pb/^{238}U$ age of 601.7 ± 1.3 Ma and a $^{207}Pb/^{206}Pb$ age of 607 ± 4 Ma. Using 91500 as the primary standard, 258 analyses of GJ-1 zircon yield a $^{206}Pb/^{238}U$ weighted mean age of 602.7 ± 0.5 Ma (MSWD = 1.2; 5 rejected) and a $^{207}Pb/^{206}Pb$ weighted mean age of 605.5 ± 1.8 Ma (MSWD = 1.0), both statistically indistinguishable from the TIMS ages. The REE + Hf concentrations are rather homogeneous and comparable to those reported by Liu et al. (2010).

The Plešovice RM (337.13 ± 0.37 Ma; Slama et al., 2008), was analyzed 170 times over the course of this study and yielded a $^{206}Pb/^{238}U$ weighted mean age of 340.7 ± 0.3 Ma (MSWD = 0.9; 5 rejected) and a $^{207}Pb/^{206}Pb$ weighted mean age of 335.7 ± 2.4 Ma (MSWD = 1.0). The mean $^{206}Pb/^{238}U$ and $^{207}Pb/^{206}Pb$ ages are dissimilar to each other and to those reported by Slama et al. (2008). The $^{206}Pb/^{238}U$ age obtained in this study is 1% too old. This may be the result of the increased down-hole U/Pb fractionation in Plešovice compared to the other RMs: Plešovice contains up to 3000 ppm U and has undergone more radiation damage than our other reference materials and thus is ablated at a higher rate. Because the ablation pit is deeper than the other reference materials, the down-hole fractionation is greater, resulting in an elevated $^{206}Pb/^{238}U$ ratio. $^{207}Pb/^{206}Pb$ ratios are not fractionated with pit depth. Plešovice REE + Hf concentrations are more variable than 91500 and GJ-1, and in accordance with those reported by Slama et al. (2008).

Our other zircon RMs yielded results similar to published values, with $^{206}Pb/^{238}U$ weighted mean ages within 0.5% of the reference value: 1103.4 ± 5.4 Ma (25 of 25; MSWD = 2.2) for FC-1 (1099.3 ± 0.7; Paces and Miller, 1993), 566.6 ± 0.7 Ma (57 of 57; MSWD = 1.0) for SL1 (563.5 ± 3.2 Ma; Gehrels, 2000), 417.7 ± 0.8 Ma (69 of 71; MSWD = 1.7) for R33 (416.29 ± 0.39 Ma; Black et al., 2004), 567.1 ± 1.4 Ma (36 of 38; MSWD = 1.5) for Peixe (564 ± 4; Dickinson and Gehrels, 2003), and 533.4 ± 2.1 Ma (19 of 19; MSWD = 1.3) for Seiland (531 ± 2; Pedersen et al., 1989). All mean ages for the secondary RMs are older than their respective published mean age, indicating, perhaps, that our primary RM (91500) is nearly 0.5% older than its published value. The REE + Hf concentrations are more variable for the ternary RMs, but the patterns for a single sample are consistent (e.g., Eu/Eu^*, Lu/Dy; Fig. 5); concentrations of R33 are similar to published values (Black et al., 2004).

4.1.2. Hf (MC-ICP) + U–Pb ± REE (SC-ICP) data

Another possible LASS configuration is to measure REE and/or U–Pb on the AttoM and Hf isotopic compositions on the Plasma (Figs. 4 and 7; Tables DR4 and DR5). When only U–Th–Pb are measured on the AttoM, the $^{206}Pb/^{238}U$ ages for individual 50 μm spot analyses have uncertainties of 1–2% depending on U and Pb concentrations. The weighted mean $^{206}Pb/^{238}U$ ages are within ~1% of the published values: GJ-1 yielded 607.8 ± 1.7 Ma and the Mud Tank zircon (732 Ma; Black and Gulson, 1978) yielded 726.7 ± 2.5 Ma. When U–Th–Pb *and* trace-element data are obtained on the AttoM, uncertainties on the $^{206}Pb/^{238}U$ age of individual spots climb to ~6–7% (Fig. 3). In this case, GJ-1 is still accurate (605.9 ± 7.6 Ma; n = 24; MSWD = 0.5), whereas Mud Tank yields an age >2% younger than the published age (716.8 ± 9.7 Ma; n = 24;

Table 2
Mass position configurations for Nu Plasma.

Configuration	ExH	H2	H1	Ax	L1	L2	L3	L4	L5	L6	L7	L8	IC0	IC1	IC2	IC3
1	238	232											208	207	206	204
2	238	232								208	207	206	204		202	200
3			180	179	178	177	176	175	174	173	172	171				

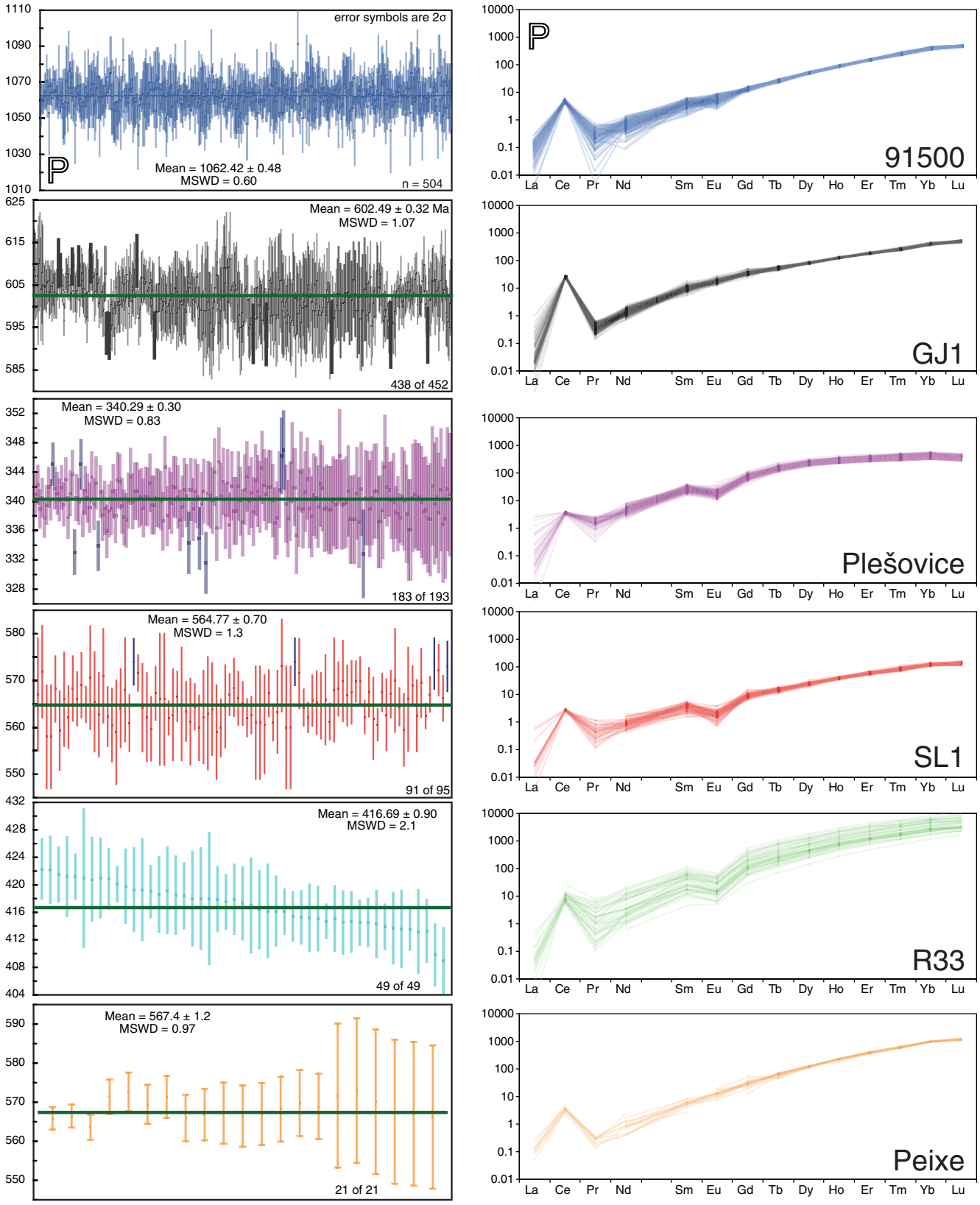

Fig. 5. LASS (U–Pb + REE) data for zircon reference materials. The primary standard ("P") used in this study is 91500.

MSWD = 0.6). REE concentrations for GJ-1 and Mud Tank are comparable to published values (Yuan et al., 2008; Liu et al., 2010).

Fig. 7 shows data obtained during simultaneous measurement of U–Th–Pb on the AttoM and Hf on the Plasma. Uncertainties for individual analyses depend on spot size, depth, and Hf concentration; the uncertainty steadily decreases as sample size is increased to 1500 ng (>0.06%–0.04%, 2σ), but beyond this, there is little improvement in precision (max ~0.035%, 2σ). Replicate analyses yield $^{176}Hf/^{177}Hf$ within error of published values: 0.282283 ± 19 (n = 49, MSWD = 0.99) for 91500 (0.282284 ± 3; Wiedenbeck et al., 1995), 0.282008 ± 17

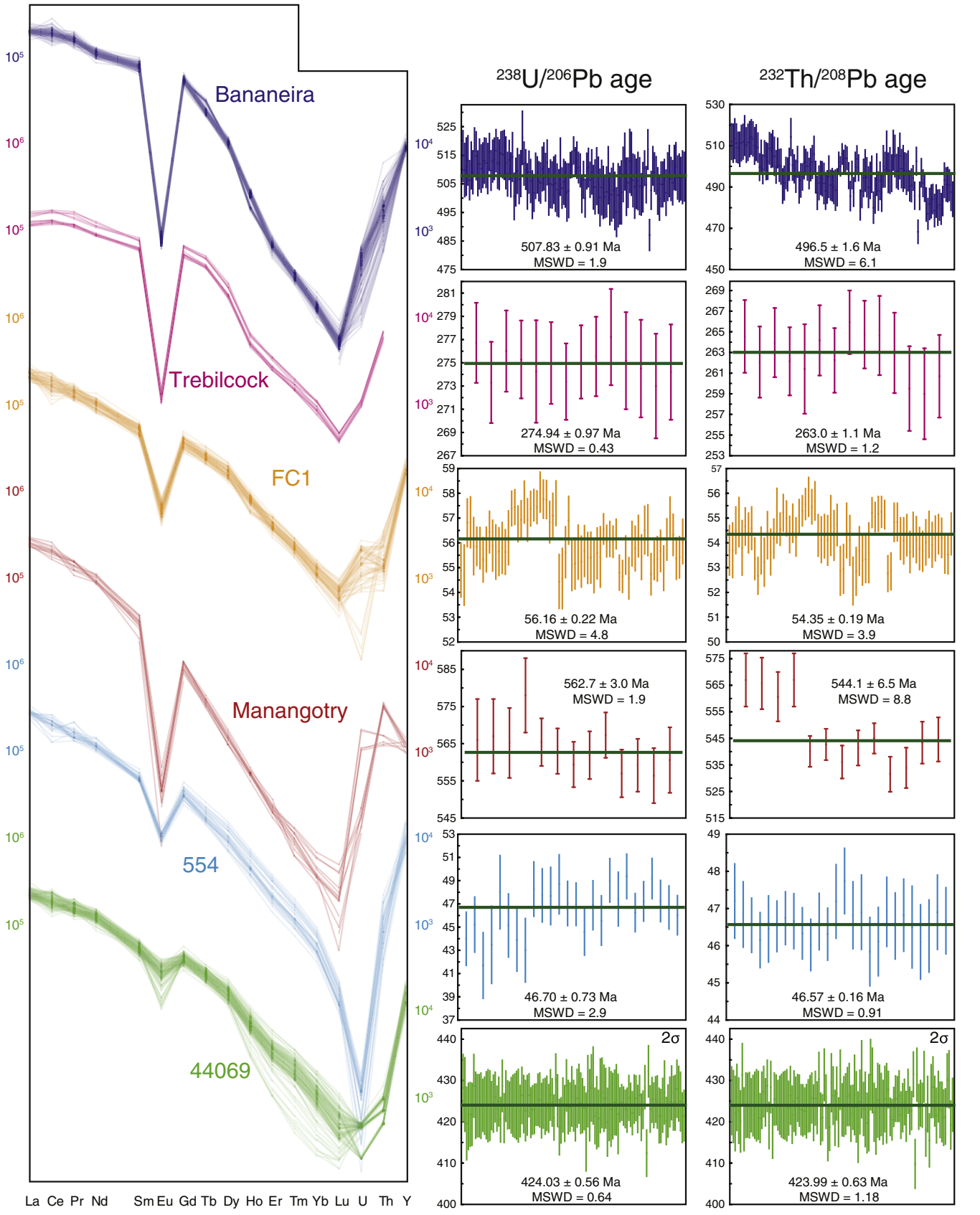

Fig. 6. LASS data for monazite reference materials. Bananeira was the primary standard for trace element data; 44069 was used as the primary standard for U–Th–Pb data.

(n = 47, MSWD = 1.02) for GJ-1 (0.282000 ± 0.0000005, Morel et al., 2008), and 0.282507 ± 15 (n = 48, MSWD = 0.76) for Mud Tank (0.282507 ± 0.000006, Woodhead and Hergt, 2005). An MSWD of unity for all three samples indicates that calculated uncertainties for individual spot analyses represents the total uncertainty in each measurement, i.e., there is no excess external uncertainty.

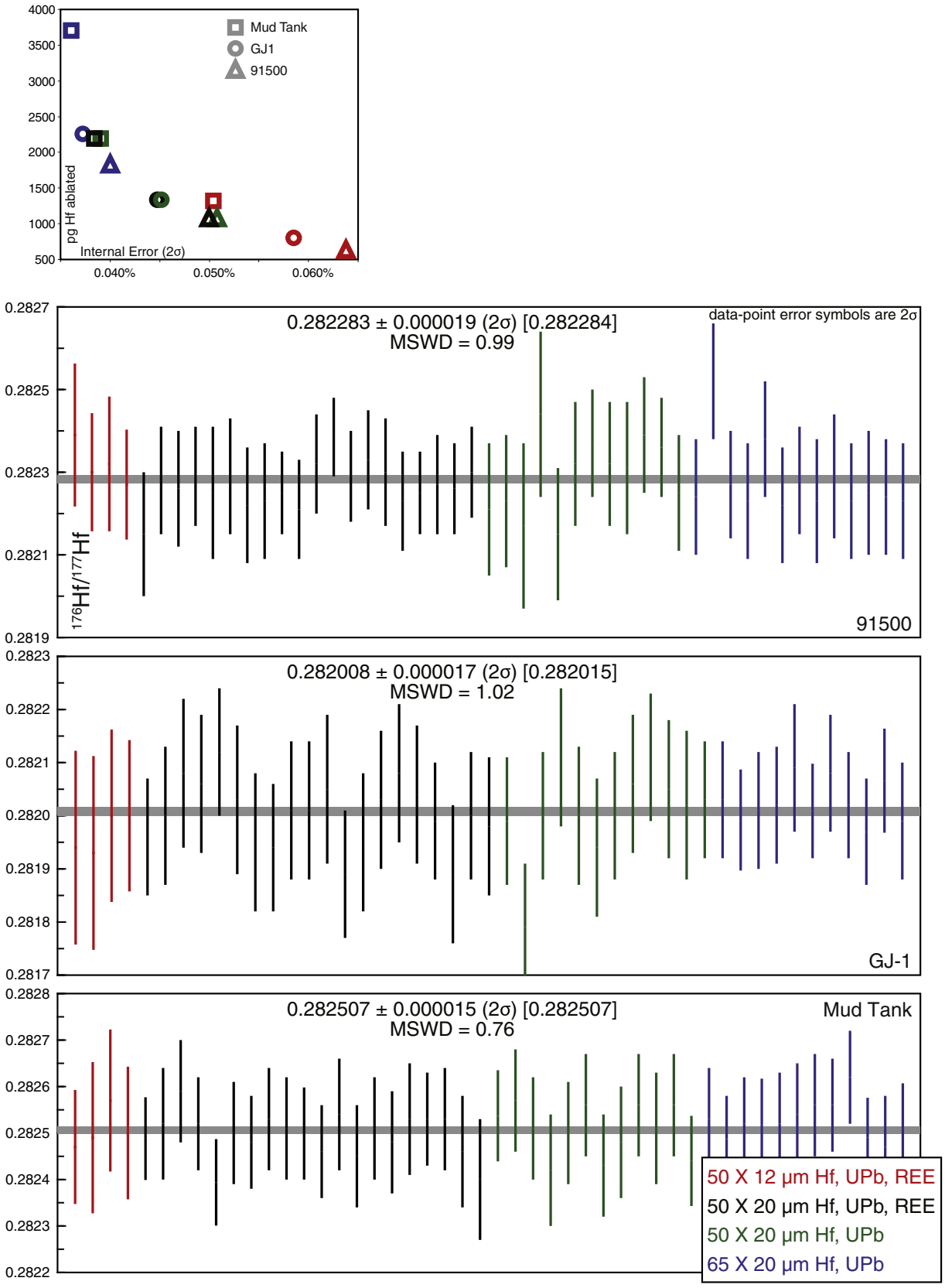

Fig. 7. Hf portion of LASS data for Hf, U/Pb ± REE. Published values are listed in brackets. Uncertainties decrease steadily with increasing total Hf yield until ~1500 pg, at which point an increase in precision with increase Hf yield is increasingly diminished.

4.2. Monazite

In a similar manner to the zircon reference materials, here we report analyses of multiple monazite reference materials measured over a one-year period (2011): 44069 (Aleinikoff et al., 2006); Bananeira (Supplied by Richard Stern: ~512 Ma), FC1 (56 Ma, Horstwood et al., 2003), Manangotry (553 Ma; Horstwood et al., 2003), Trebilcock (272 Ma, Tomascak et al., 1996), and 554 (44–47 Ma, Shakel et al., 1977). Of these samples, only one sample has been analyzed for its Th–Pb age: 554 (45 Ma, measured by M. Tatsumoto, cited in Harrison et al., 1999). The majority of data reported are from reference materials 44069, Bananeira, and FC1; these were used as the primary and secondary standards within most analytical sessions. The 44069 reference material was used as the primary standard for U–Th–Pb and the Bananeira monazite was used as the primary standard for TE concentrations; all other reference materials were treated as unknowns, and therefore demonstrate the accuracy of the LASS results. U–Pb and trace-element are presented in Tables DR1 and DR6 and Fig. 6.

4.2.1. U–Th–Pb (MC-ICP) + trace-element (SC-ICP) data

The primary U–Th–Pb chronometric standard used in this study is the 44069 monazite, which yields both a $^{206}Pb/^{238}U$ and $^{207}Pb/^{235}U$ age of ~424.9 Ma (Aleinikoff et al., 2006). Because no isotope-dilution data exist for the Th–Pb age for 44069, we used an assumed age of 425 Ma. The long-term average of 44069 was 424.9 ± 0.6 Ma (0.13% 2SE, MSWD = 0.64), 424.8 ± 0.5 (0.13% 2SE, MSWD = 0.64), and 424.9 ± 0.6 (0.14% 2SE, MSWD = 1.18), for the $^{206}Pb/^{238}U$, $^{207}Pb/^{235}U$, and $^{208}Pb/^{232}Th$ ages, respectively.

The Bananeira monazite reference material yielded a $^{206}Pb/^{238}U$ age of 508.9 ± 0.9 (0.18% 2SE, MSWD = 1.9), and a $^{208}Pb/^{232}Th$ age of 497.6 ± 1.6 (0.32% 2SE, MSWD = 6.1), and FC1 yielded a $^{206}Pb/^{238}U$ age of 56.3 ± 0.2 (0.38% 2SE, MSWD = 4.6), and a $^{208}Pb/^{232}Th$ age of 54.5 ± 0.2 (0.35% 2SE, MSWD = 3.9). The Manangotry reference material yielded a $^{206}Pb/^{238}U$ age of 563.9 ± 3.0 (0.53% 2SE, MSWD = 1.9) and a $^{208}Pb/^{232}Th$ age of 545.3 ± 6.5 (1.2% 2SE, MSWD = 8.8). Treblicock monazite yielded a $^{206}Pb/^{238}U$ age of 275.3 ± 1.0 (0.36% 2SE, MSWD = 0.4) and a $^{208}Pb/^{232}Th$ age of 263.7 ± 1.0 (0.36% 2SE, MSWD = 1.2), and 554 yielded a common-Pb corrected $^{206}Pb/^{238}U$ age of 46.8 ± 0.7 (1.6% 2SE, MSWD = 2.9) and a $^{208}Pb/^{232}Th$ age of 46.7 ± 0.2 (0.35% 2SE, MSWD = 0.9).

With the exception of the Manangotry monazite, all secondary reference materials yielded individual spot analyses within 3% of the accepted ID-TIMS value and weighted mean $^{206}Pb/^{238}U$ ages within 1% of their accepted ID-TIMS values. $^{208}Pb/^{232}Th$ ages are harder to evaluate, because there exists only one ID-TIMS value. Using 44069 as the primary standard yields $^{208}Pb/^{232}Th$ ages for of *all* secondary standards that are younger than their $^{206}Pb/^{238}U$ ages. This implies that the $^{208}Pb/^{232}Th$ age of 44069 is significantly older than its $^{206}Pb/^{238}U$ age; we speculate that this may be caused by either matrix effects or Th loss. Distinguishing between these two possibilities is a topic for future research.

Older samples tend to have more spot to spot scatter (i.e., a higher MSWD) in the $^{208}Pb/^{232}Th$ ratio than in the $^{206}Pb/^{238}U$ ratio, whereas the scatter is high for both ratios in young samples. We attribute this to more-limited accuracy in the $^{208}Pb/^{232}Th$ ratios vs. $^{206}Pb/^{238}U$ ratios; because minor age variation in older standards is swamped by measurement precision (e.g., 1 Myr variation in FC1 is 2%, whereas 1 Myr variation in Bananeira is 0.2%), scatter in the $^{206}Pb/^{238}U$ age is less in older samples. Inaccuracy in the $^{208}Pb/^{232}Th$ ratio is greater than that for $^{206}Pb/^{238}U$, such that the scatter in $^{208}Pb/^{232}Th$ ratios is similar between old and young samples. A similarly larger MSWD in the $^{208}Pb/^{232}Th$ ratios vs. $^{206}Pb/^{238}U$ ratios is also displayed in the zircon data. We attribute the $^{208}Pb/^{232}Th$ analytical limitations to 1) heterogeneity in our primary reference material, and/or 2) greater sensitivity in the fractionation of Th relative to U and Pb due to external factors such as laser energy, gas flow, and plasma flicker.

5. LASS as a petrochronometer: examples from (U)HP metamorphic terranes

The capabilities of the LASS technique can be suitably exemplified through its application to deconvolve the complicated history of ultrahigh-pressure terranes—exhumed slices of continental material once subducted into the coesite-stability field—because the geologic history involves a variety of rock types with multiple petrochronometers and occurred over a broad range of temperatures and pressures, such that different chronometers record different parts of the rock history. This section explores the change in chemical signatures of zircon and monazite within and among samples from a few different UHP terranes and evaluates how these signatures allow us to distinguish the timing of events during the subduction and exhumation of continental crust.

5.1. Western Gneiss Region, Norway

The Western Gneiss Region (WGR) is one of the two giant UHP terranes (~30,000 km^2), and formed via the westward subduction of Baltica and overlying allochthons beneath the Laurentian craton and subsequent eastward exhumation during the Caledonian orogeny (for a review, see Hacker et al., 2000). Subduction initiated prior to 420 Ma, high-pressure conditions lasted through ~400 Ma, and exhumation and cooling ensued though ~380 Ma (Carswell et al., 2003; Tucker et al., 2004; Walsh and Hacker, 2004; Root et al., 2005; Kylander-Clark et al., 2007; Kylander-Clark, 2008; Kylander-Clark et al., 2009; Krogh et al., 2011). Here we present data from a single sample from the WGR—the eclogite at Midsund Bruk described and dated using conventional TIMS methods by Krogh et al. (2011). Krogh et al. obtained isotopic ratios with $^{206}Pb/^{238}U$ dates from 420 to 405 Ma from five single-grain and multi-grain separates. All five isotopic ratios yield a well-constrained lower intercept date of 397.5 ± 9.0 Ma, but Krogh et al. chose the most-concordant and youngest datum with a $^{206}Pb/^{238}U$ date of 405 ± 1 Ma as the minimum age of the eclogite-facies metamorphism. LASS analysis zircons from the same zircon separates (provided by S. Kamo, P. Robinson, and M. Terry) produced data with a similar range of $^{206}Pb/^{238}U$ dates—420.6 ± 1.3 Ma to 400.4 ± 1.7 Ma (Fig. 8)—but with three distinct chemical signatures correlated to three different date ranges. The lack of a steep, positive HREE pattern and negative Eu anomaly in all spot analyses contrasts with typical igneous zircons and implies that zircon grew in the presence of garnet and absence of plagioclase (see Zircon petrochronology, above) for at least 20 Myr. The differences in the REE patterns of the three distinct groups are likely the result of (re)crystallization during reactions with different minerals, in the presence of different fluids, or at different diffusive lengthscales. For example, the early crystallization of the MREE-rich zircon at ~420 Ma could have occurred as epidote, or perhaps titanite, was decomposing. In this case the LASS data show that the variation of $^{206}Pb/^{238}U$ dates obtained by TIMS is real and reflects protracted (re)crystallization under changing conditions.

Petrochronologic data from monazite from UHP rocks can complement that of zircon, as exemplified in Fig. 9. The monazite from a garnet–muscovite–kyanite gneiss at Leinøya exhibits 4 distinct compositional/date groups: 1) moderate Sr, low Eu/Eu^* and HREE material with a weighted mean of 426.5 ± 5.6 Ma; 2) high Sr, low Eu/Eu^* and HREE with a date of 408.8 ± 6.3 Ma; 3) low Sr, low Eu/Eu^* and HREE with an date of 395.0 ± 3.9 Ma; and 4) low Sr and Eu/Eu^*, and relatively high HREE with a date of 390.3 ± 4.9 Ma. The depletion of HREE of groups 1–3 implies monazite growth in the presence of garnet from ~426–395 Ma. The increase and subsequent decrease in Sr from group 1–2 and 2–3 respectively, implies the breakdown and reappearance of plagioclase as the sample traveled into and out of eclogite-facies conditions after ~426 Ma and prior to ~390 Ma, respectively. The final composition/date group suggests that garnet began breaking down as plagioclase continued to grow as late as 390 Ma.

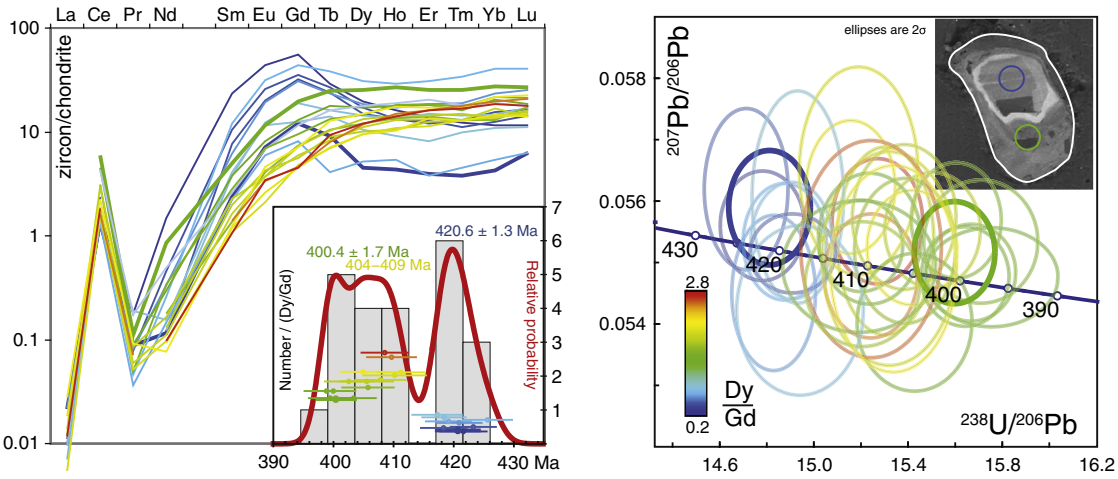

Fig. 8. U–Pb and REE data for the Midsund Bruk eclogite (TK9817; Krogh et al., 2011). Old metamorphic dates have negative MREE slopes, whereas later zircon dates are characterized by a steep MREE slope that decreases with age. Cathodoluminescence image of zircon reveals both metamorphic zircon episodes; 24 μm analysis spots correspond to boldface age and REE data.

Together the zircon and monazite data from the two UHP samples imply that eclogite-facies metamorphism lasted from ~420–400 Ma (Fig. 10). Garnet-stable metamorphism was underway by at least ~426 Ma, and decompression through garnet–amphibolite facies occurred through ~394 Ma and ended by ~390 Ma. These data are consistent with the relative timing of events determined in numerous studies (referenced above) and yet were obtained from only two samples.

5.2. Saidenbach diamond-bearing gneiss, Bohemian Massif

The Saidenbach locality in the Erzgebirge Crystalline Complex contains a few diamondiferous gneiss lenses (few km^2 total area) interpreted to represent UHP subducted metasedimentary rock (Massonne, 2003). Massonne et al. (2007) presented ages from 3 distinct zones of zircon: 1) HP cores (337.0 ± 2.7 Ma), 2) UHP mantles (336.8 ± 2.8 Ma), and 3) HP rims (330.2 ± 5.8). Monazites in the same study yielded SIMS ages of ~332 Ma.

We analyzed zircon and monazite from the same diamondiferous gneiss using LASS. The zircon LASS data show two chemically distinct zones that have dates that are equivalent at the 2σ level (Fig. 11). The cores have a mean $^{206}Pb/^{238}U$ date of 341.8 ± 2.0 Ma and lower LREE and higher HREEs than the diamond-bearing rims (340.1 ± 1.8 Ma). These two compositions/date signatures are likely equivalent to zones 1 and 2 of Massonne et al. (2007). The two distinct compositions/date signatures could correspond to 1) (re)crystallization of zircon in the presence of garnet and 2) UHP (re)crystallization of zircon during the breakdown of a LREE-rich phase (e.g., monazite, apatite, or titanite). More than 50 LASS analyses of monazite—including transects across a ~1 mm grain—yield similar REE signatures, which, because of the low abundance of HREE, suggest garnet stable growth, and a single-population date of 336.1 ± 0.7 Ma. In total, the LASS data from the

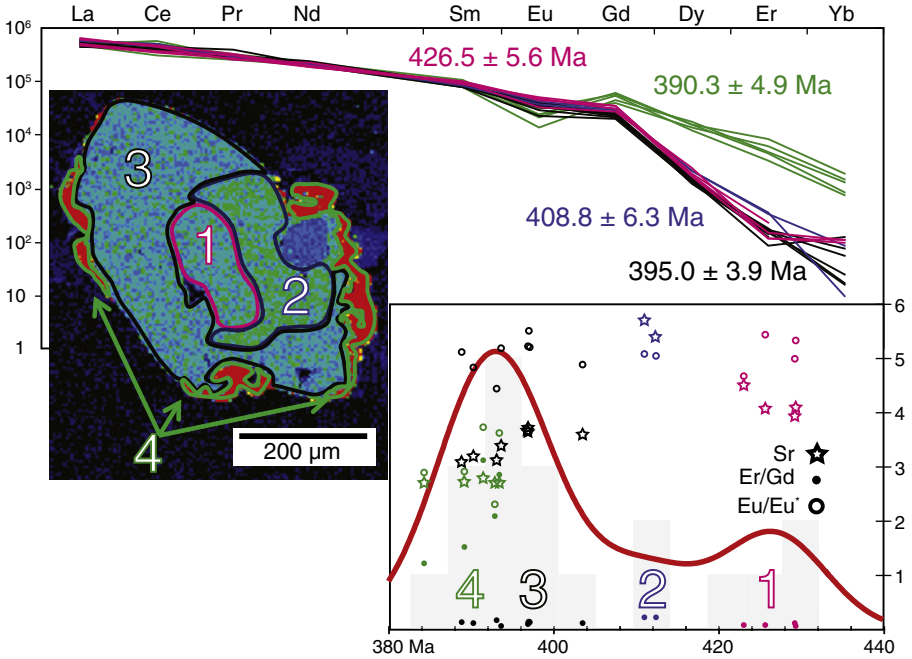

Fig. 9. Trace-element REE and age data for monazite from the Leinøya UHP gneiss. Yttrium map shows 4 distinct (re)crystallization domains, corresponding to 4 distinct age/chemical domains.

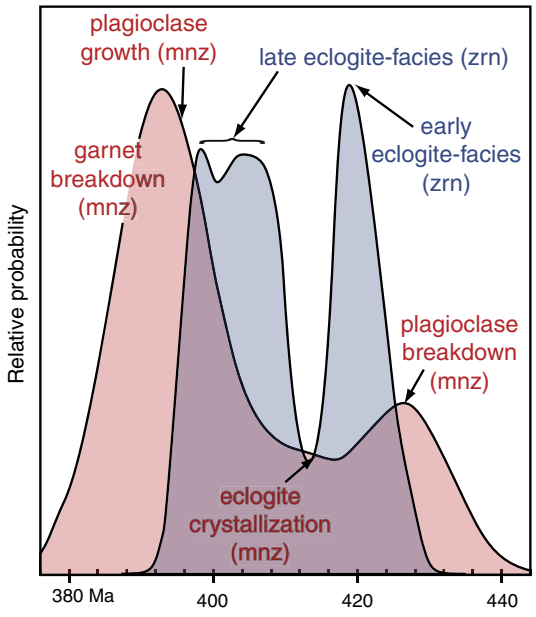

Fig. 10. Probability density plots of Leinøya UHP gneiss monazite and Midsund Bruk eclogite zircon demonstrate the ability of LASS to deconvolve the complicated history of a metamorphic terrane rapidly and effectively.

Saidenbach locality indicate 3 distinct periods of zircon and monazite (re)crystallization during short-term crustal burial and exhumation and illustrate the benefit of LASS analyses over conventional methods: rapid and accurate throughput provides abundant, meaningful data that can be used to understand the timing and nature of geological phenomena (Graham & Trotman, Londo).

6. Summary

Petrochronology is the simultaneous use of geochronology and geochemistry to address geologic problems that cannot be solved by either technique in isolation. Under typical circumstances, petrochronology enables a date derived from isotopic ratios to be tied directly to a particular mineral paragenesis or mineral composition(s), and—under ideal circumstances—to a particular pressure, temperature, and/or fluid activity or composition. Well-known qualitative examples include the use of Y or HREE depletion to infer the presence of garnet during the time represented by the isotopic date, or the use of a negative europium anomaly to infer the presence of feldspar. Quantitative examples include thermometry based on Ti solubility in zircon and Zr solubility in rutile and titanite. Much work, such as the assessment of element partitioning as a function of pressure, temperature, bulk composition, and mineral assemblage, remains to be done to extend the application to a broader range of elements and minerals.

A variety of petrochronology techniques have been developed; the most recent is the simultaneous analysis of a laser-ablation particle stream on a multi-collector, double-focusing ICPMS and a single-collector, double-focusing ICPMS. This configuration combines the high spatial precision of laser ablation (10–30 μm spot diameter) with the high isotopic ratio precision and accuracy of multi-collector ICPMS and the high sensitivity of single-collector ICPMS.

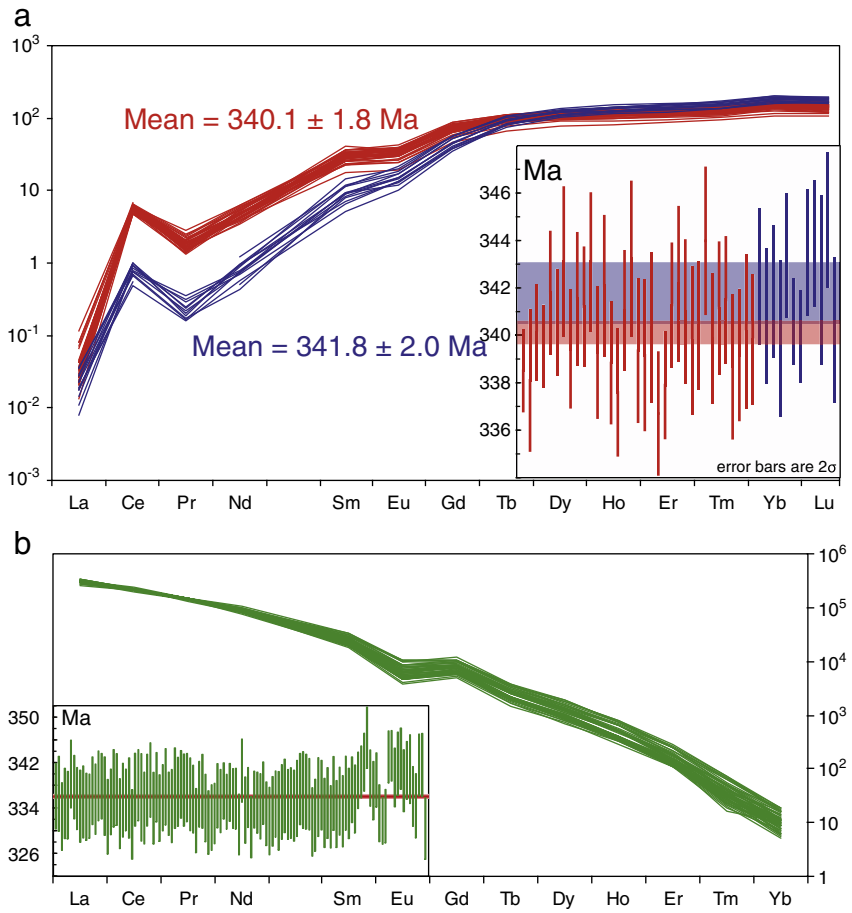

Fig. 11. a. Zircon LASS data from the Saidenbach diamond-bearing gneiss. The two compositional distinct groups have indistinguishable ages. b. Monazite LASS data from the Saidenbach diamond-bearing gneiss. Similar chemistry and a single age population from numerous monazites imply that monazite (re)crystallization was rapid.

Acknowledgments

This project was funded by NSF grants EAR-0923552 and EAR-0911485 to Hacker and EAR-1050043 to Cottle, and the University of California, Santa Barbara. This manuscript was improved through the thoughtful input of two anonymous reviewers.

Appendix A. Supplementary data

Supplementary data to this article can be found online at http://dx.doi.org/10.1016/j.chemgeo.2013.02.019.

References

Ahrens, L.H., 1965. Some observations on the uranium and thorium distributions in accessory zircon from granitic rock. Geochimica et Cosmochimica Acta 29, 711–716.
Ahrens, L.H., Cherry, R.D., Erlank, A.J., 1967. Observations on the Th–U relationship in zircons from granitic rocks and from kimberlites. Geochimica et Cosmochimica Acta 31 (12), 2379–2387.
Aleinikoff, J.N., et al., 2006. Deciphering igneous and metamorphic events in high-grade rocks of the Wilmington Complex, Delaware; morphology, cathodoluminescence and backscattered electron zoning, and SHRIMP U–Pb geochronology of zircon and monazite. Geological Society of America Bulletin 118 (1–2), 39–64.
Ayers, J.C., Miller, C., Gorisch, B., Milleman, J., 1999. Textural development of monazite during high-grade metamorphism: hydrothermal growth kinetics, with implications for U, Th–Pb geochronology. American Mineralogist 84, 1766–1780.
Bea, F., Montero, P., Garuti, G., Zacharini, F., 1998. Pressure-dependence of rare earth element distribution in amphibolite- and granulite-grade garnets. An LA-ICP-MS study. Geostandards Newsletter 21, 253–270.
Bell, T.H., Welch, P.W., 2002. Prolonged Acadian orogenesis; revelations from foliation intersection axis (FIA) controlled monazite dating of foliations in porphyroblasts and matrix. American Journal of Science 302 (7), 549–581.
Belousova, E.A., Griffin, W.L., O'Reilly, S.Y., Fisher, N.I., 2002. Igneous zircon; trace element composition as an indicator of source rock type. Contributions to Mineralogy and Petrology 143 (5), 602–622.
Berger, A., Scherrer, N.C., Bussy, F., 2005. Equilibration and disequilibration between monazite and garnet; indication from phase-composition and quantitative texture analysis. Journal of Metamorphic Geology 23 (9), 865–880.
Bingen, B., van Breemen, O., 1998. U–Pb monazite ages in amphibolite- to granulite-facies orthogneisses reflect hydrous mineral breakdown reactions: Sveconorwegian Province of SW Norway. Contributions to Mineralogy and Petrology 132, 336–353.
Bingen, B., Austrheim, H., Whitehouse, M., 2001. Ilmenite as a source for zirconium during high-grade metamorphism? Textural evidence from the Caledonites of Norway and implications for zircon geochronology. Journal of Petrology 42, 355–375.
Black, L.P., Gulson, B.L., 1978. The age of the Mud Tank Carbonatite, Strangways Range, Northern Territory. BMR Journal of Australian Geology and Geophysics 3 (3), 227–232.
Black, L.P., et al., 2004. Improved $^{206}Pb/^{238}U$ microprobe geochronology by the monitoring of a trace-element-related matrix effect; SHRIMP, ID-TIMS, ELA-ICP-MS and oxygen isotope documentation for a series of zircon standards. Chemical Geology 205 (1–2), 115–140.
Burt, D.M., 1989. Compositional and phase relations among rare earth element minerals. Reviews in Mineralogy 21, 59–307.
Carswell, D.A., Brueckner, H.K., Cuthbert, S.J., Mehta, K., O'Brien, P.J., 2003. The timing of stabilisation and the exhumation rate for ultra-high pressure rocks in the Western Gneiss Region of Norway. Journal of Metamorphic Geology 21, 601–612.
Catlos, E.J., Gilley, L.D., Harrison, T.M., 2002. Interpretation of monazite ages obtained via in situ analysis. Chemical Geology 140.
Chaudhuri, J.N.B., Newesely, H., 1993. On the REE-bearing minerals in the beach placers of Puri. Orissa District Journal of Southeast Asian Earth Science 8, 287–291.
Chen, R., Zheng, Y., Xie, L., 2010. Metamorphic growth and recrystallization of zircon; distinction by simultaneous in situ analyses of trace elements, U/Th/Pb and Lu/Hf isotopes in zircons from eclogite facies rocks in the Sulu Orogen. Lithos 114 (1–2), 132–154.
Cherniak, D.J., Pyle, J.M., 2008. Th diffusion in monazite. Chemical Geology 256 (1–2), 52–61.
Cherniak, D.J., Watson, E.B., 2003. Diffusion in zircon. Reviews in Mineralogy and Geochemistry 53, 113–144.
Cherniak, D.J., Watson, E.B., Grove, M., Harrison, T.M., 2004. Pb diffusion in monazite: a combined RBS/SIMS study. Geochimica et Cosmochimica Acta 68, 829–840.
Corfu, F., Hanchar, J.M., Hoskin, P.W.O., Kinny, P.D., 2003. Atlas of zircon textures. Reviews in Mineralogy and Geochemistry 53, 469–500.
Corrie, S.L., Kohn, M.J., 2008. Trace element distributions in silicates during prograde metamorphic reactions; implications for monazite formation. Journal of Metamorphic Geology 26 (4), 451–464.
Cottle, J.M., Horstwood, M.S.A., Parrish, R.R., 2009a. A new approach to single shot laser ablation analysis and its application to in situ Pb/U geochronology. Journal of Analytical Atomic Spectrometry. http://dx.doi.org/10.1039/b821899d.
Cottle, J.M., et al., 2009b. Geochronology of granulitized eclogites from the Ama Drime Massif, implications for the tectonic evolution of the South Tibetan Himalaya. Tectonics. http://dx.doi.org/10.1029/2008TC002256.
Cottle, J.M., Searle, M.P., Horstwood, M.S.A., Waters, D.J., 2009c. Timing of midcrustal metamorphism, melting, and deformation in the Mount Everest region of southern Tibet revealed by U(−Th)–Pb geochronology. Journal of Geology 117 (6), 643–664.
Dahl, P.S., et al., 2005. Electron probe (Ultrachron) microchronometry of metamorphic monazite; unraveling the timing of polyphase thermotectonism in the easternmost Wyoming Craton; Black Hills, South Dakota. American Mineralogist 90 (11–12), 1712–1728.
Degeling, H., Eggins, S., Ellis, D.J., 2001. Zr budgets for metamorphic reactions, and the formation of zircon from garnet breakdown. Mineralogical Magazine 65, 749–758.
DeWolf, C.P., Belshaw, N., O'Nions, R.K., 1993. A metamorphic history from micron-scale $^{207}Pb/^{206}Pb$ chronometry of Archean monazite. Earth and Planetary Science Letters 120, 207–220.
Dickinson, W.R., Gehrels, G.E., 2003. U–Pb ages of detrital zircons from Permian and Jurassic eolian sandstones of the Colorado Plateau, USA; paleogeographic implications. Sedimentary Geology 163 (1–2), 29–66.
Dumond, G., Goncalves, P., Williams, M.L., Jercinovic, M.J., 2006. Subhorizontal fabric in exhumed continental lower crust and implications for lower crustal flow; Athabasca granulite terrane, western Canadian Shield. Tectonics 29 (2), 2010.
Eggins, S.M., Rudnick, R.L., McDonough, W.F., 1998. The composition of peridotites and their minerals; a laser-ablation ICP-MS study. Earth and Planetary Science Letters 154 (1–4), 53–71.
Eggins, S., et al., 2005. In situ U-series dating by laser-ablation MC-ICPMS. Geochimica et Cosmochimica Acta 69 (10, Suppl.), 377.
Eskova, E.M., 1959. K geokhimii Nb i Ta v massivakh nefelinovykh sienitov Vishnevykh gor. Geokhimiya 2, 130–139.
Ferry, J.M., Watson, E.B., 2007. New thermodynamic models and revised calibrations for the Ti-in-zircon and Zr-in-rutile thermometers. Contributions to Mineralogy and Petrology. http://dx.doi.org/10.1007/s00410-007-0201-0.
Finch, R.J., Hanchar, J.M., 2003. Structure and Chemistry of zircon and zircon-group minerals. Reviews in Mineralogy and Geochemistry 53, 1–25.
Finger, F., Krenn, E., 2007. Three metamorphic monazite generations in a high-pressure rock from the Bohemian Massif and the potentially important role of apatite in stimulating polyphase monazite growth along a PT loop. Lithos 95 (1–2), 103–115.
Foster, G., Kinny, P., Vance, D., Prince, C., Harris, N., 2000. The significance of monazite U–Th–Pb age data in metamorphic assemblages; a combined study of monazite and garnet chronometry. Earth and Planetary Science Letters 181, 327–340.
Foster, G., et al., 2002. Textural, chemical and isotopic insights into the nature and behaviour of metamorphic monazite. Chemical Geology 191, 183–207.
Foster, G., et al., 2004. The generation of prograde P–T–t points and paths; a textural, compositional, and chronological study of metamorphic monazite. Earth and Planetary Science Letters 228, 125–142.
Franz, G., Andrehs, G., Rhede, D., Ayora, C., 1996. Crystal chemistry of monazite and xenotime from Saxothuringian–Moldanubian metapelites, NE Bavaria, Germany. European Journal of Mineralogy 8 (5), 1097–1118.
Fraser, G., Ellis, D., Eggins, S., 1997. Zirconium abundance in granulite-facies minerals, with implications for zircon geochronology in high-grade rocks. Geology 25, 607–610.
Frondel, C., 1953. Hydroxyl substitution in thorite and zircon. American Mineralogist 38 (11–12), 1007–1018.
Gehrels, G.E., 2000. Introduction to detrital zircon studies of Paleozoic and Triassic strata in western Nevada and Northern California. Special Paper — Geological Society of America 347, 1–17.
Gerdes, A., Liu, F., Weyer, S., Brey, G., Anonymous, 2007. Chronological history of UHP rocks from the Chinese Continental Scientific Drilling; a multi-methodical approach. Geochimica et Cosmochimica Acta 71 (15S), A317.
Gibson, H.D., Carr, S.D., Brown, R.L., Hamilton, M.A., 2004. Correlations between chemical and age domains in monazite, and metamorphic reactions involving major pelitic phases; an integration of ID-TIMS and SHRIMP geochronology with Y–Th–U X-ray mapping. Chemical Geology 211, 237–260.
Giere, R., Sorensen, S.S., 2004. Allanite and other REE-rich epidote-group minerals. Reviews in Mineralogy and Geochemistry 56, 431–493.
Goncalves, P., Williams, M.L., Jercinovic, M.J., Tracy, R.J., 2005. Electron-microprobe age mapping of monazite. American Mineralogist 90 (4), 578–585.
Gramaccioli, C.M., Segalstad, T.V., 1978. A uranium- and thorium-rich monazite from a south-alpine pegmatite at Piona, Italy. American Mineralogist 63, 757–761.
Gromet, L.P., Silver, L.T., 1983. Rare earth element distributions among minerals in a granodiorite and their petrogenetic implications. Geochimica et Cosmochimica Acta 47 (5), 925–940.
Hacker, B.R., et al., 2000. Hot and dry xenoliths from the lower crust of Tibet. Science 287, 2463–2466.
Hanchar, J.M., Rudnick, R.L., 1995. Revealing hidden structures; the application of cathodoluminescence and back-scattered electron imaging to dating zircons from lower crustal xenoliths. Lithos 36 (3–4), 289–303.
Hanchar, J.M., et al., 2001. Rare earth elements in synthetic zircon; part 1, synthesis, and rare earth element and phosphorus doping. American Mineralogist 86 (5–6), 667–680.
Harrison, T.M., McKeegan, K.D., Le Fort, P., 1995. Detection of inherited monazite in the Manaslu leucogranite by $^{208}Pb/^{232}Th$ ion microprobe dating. Earth and Planetary Science Letters 133, 271–282.
Harrison, T.M., et al., 1999. Origin and episodic emplacement of the Manaslu intrusive complex, Central Himalaya. Journal of Petrology 40 (1), 3–19.
Hawkins, D.P., Bowring, S.A., 1997. U–Pb systematics of monazite and xenotime: case studies from the Paleoproterozoic of the Grand Canyon, Arizona. Contributions to Mineralogy and Petrology 127, 87–103.
Hermann, J., Rubatto, D., 2003. Relating zircon and monazite domains to garnet growth zones; age and duration of granulite facies metamorphism in the Val Malenco lower crust. Journal of Metamorphic Geology 21, 833–852.
Hermann, J., Rubatto, D., Korsakov, A., Shatsky, V.S., 2001. Multiple zircon growth during fast exhumation of diamondiferous, deeply subducted continental crust

(Kokchetav Massif, Kazakhstan). Contributions to Mineralogy and Petrology 141, 66–82.
Hinton, R., Upton, B., 1991. The chemistry of zircon: variations within and between large crystals from syenite and alkali basalt xenoliths. Geochimica et Cosmochimica Acta 55, 3287–3302.
Hoisch, T.D., Wells, M.L., Grove, M., 2008. Age trends in garnet-hosted monazite inclusions from upper amphibolite facies schist in the northern Grouse Creek Mountains, Utah. Geochimica et Cosmochimica Acta 72 (22), 5505–5520.
Hokada, T., Harley, S., 2004. Zircon growth in UHT leucosome: constraints from zircon–garnet rare earth elements (REE) relations in Napier Complex, East Antarctica. Journal of Mineralogical and Petrological Sciences 99, 180–190.
Horstwood, M.S.A., Foster, G.L., Parrish, R.R., Noble, S.R., Nowell, G.M., 2003. Common-Pb corrected in situ U–Pb accessory mineral geochronology by LA-MC-ICP-MS. Journal of Analytical Atomic Spectrometry 18, 837–846.
Hoskin, P.W.O., Ireland, T.R., 2000. Rare earth element chemistry of zircon and its use as a provenance indicator. Geology 28, 627–630.
Hoskin, P.W.O., Schaltegger, U., 2003. The composition of zircon and igneous and metamorphic petrogenesis. Reviews in Mineralogy and Geochemistry 53, 27–62.
Jackson, S.E., Pearson, N.J., Griffin, W.L., Belousova, E.A., 2004. The application of laser ablation-inductively coupled plasma-mass spectrometry to in situ U/Pb zircon geochronology. Chemical Geology 211 (1–2), 47–69.
Janots, E., et al., 2008. Prograde metamorphic sequence of REE minerals in pelitic rocks of the Central Alps; implications for allanite–monazite–xenotime phase relations from 250 to 610 degrees C. Journal of Metamorphic Geology 26 (5), 509–526.
Janots, E., et al., 2009. Metamorphic rates in collisional orogeny from in situ allanite and monazite dating. Geology 37, 11–14.
Katayama, I., Ohta, M., Ogasawara, Y., 2002. Mineral inclusions in zircon from diamond-bearing marble in the Kokchetav massif, northern Kazakhstan. European Journal of Mineralogy 14, 1103–1108.
Kelly, N.M., Clarke, G.L., Harley, S.L., Baldwin, J.A., 2006. Monazite behaviour and age significance in poly-metamorphic high-grade terrains; a case study from the western Musgrave Block, central Australia. Lithos 88 (1–4), 100–134.
Kelsey, D.E., Clark, C., Hand, M., 2008. Thermobarometric modelling of zircon and monazite growth in melt-bearing systems; examples using model metapelitic and metapsammitic granulites. Journal of Metamorphic Geology 26 (2), 199–212.
Kohn, M.J., Corrie, S.L., 2011. Preserved Zr-temperatures and U–Pb ages in high-grade metamorphic titanite; evidence for a static hot channel in the Himalayan orogen. Earth and Planetary Science Letters 311 (1–2), 136–143.
Kohn, M.J., Malloy, M.A., 2004. Formation of monazite via prograde metamorphic reactions among common silicates: Implications for age determinations. Geochimica et Cosmochimica Acta 68, 101–113.
Kohn, M.J., Wieland, M.S., Parkinson, C.D., Upreti, B.N., 2005. Five generations of monazite in Langtang gneisses; implications for chronology of the Himalayan metamorphic core. Journal of Metamorphic Geology 23, 399–406.
Konzett, J., Armstrong, R.A., Sweeney, R.J., Compston, W., 1998. The timing of MARID metasomatism in the Kaapvaal mantle; an ion probe study of zircons from MARID xenoliths. Earth and Planetary Science Letters 160 (1–2), 133–145.
Krogh, T.W., Kamo, S.L., Robinson, P., Terry, M.P., Kwok, K., 2011. U–Pb zircon geochronology of eclogites from the Scandian Orogen, northern Western Gneiss Region, Norway: 14–20 million years between eclogite crystallization and return to amphibolite-facies conditions. Canadian Journal of Earth Sciences 48 (2), 441–472.
Kylander-Clark, A., 2008. Slow Subduction and Exhumation of a Thick Ultrahigh-Pressure Terrane: Western Gneiss Region, Norway. Ph.D. dissertation Thesis, University of California, Santa Barbara, 121 pp.
Kylander-Clark, A.R.C., et al., 2007. Timing of multi-stage metamorphism during ultrahigh-pressure continental subduction and exhumation: Lu/Hf and Sm/Nd geochronology in western Norway. Chemical Geology 232, 137–154.
Kylander-Clark, A.R.C., Hacker, B.R., Johnson, C.M., Beard, B.L., Mahlen, N.J., 2009. Slow subduction of a thick ultrahigh-pressure terrane. Tectonics. http://dx.doi.org/10.1029/2007TC002251.
Li, X.-H., Liang, X., Sun, M., Liu, Y., Tu, X., 2000. Geochronology and geochemistry of single-grain zircons; simultaneous in-situ analysis of U–Pb age and trace elements by LAM-ICP-MS. European Journal of Mineralogy 12 (5), 1015–1024.
Liu, D., Jian, P., Kroner, A., Xu, S., 2006. Dating of prograde metamorphic events deciphered from episodic zircon growth in rocks of the Dabie–Sulu UHP complex, China. Earth and Planetary Science Letters 250, 650–666.
Liu, Y., et al., 2010. Reappraisement and refinement of zircon U–Pb isotope and trace element analyses by LA-ICP-MS. Chinese Science Bulletin 55, 1535–1546.
Massonne, H.-J., 2003. A comparison of the evolution of diamondiferous quartz-rich rocks from the Saxonian Erzgebirge and the Kokchetav Massif: are so-called diamondiferous gneisses magmatic rocks? Earth and Planetary Science Letters 216, 347–364.
Massonne, H.J., Kennedy, A., Nasdala, L., Theye, T., 2007. Dating of zircon and monazite from diamondiferous quartzofeldspathic rocks of the Saxonian Erzgebirge; hints at burial and exhumation velocities. Mineralogical Magazine 71 (4), 407–425.
McClelland, W.C., Gilotti, J.A., Mazdab, F.K., Wooden, J.L., 2009. Trace-element record in zircons during exhumation from UHP conditions, North-East Greenland Caledonides. European Journal of Mineralogy 21 (6), 1135–1148.
McFarlane, C.R.M., Connelly, J.N., Carlson, W.D., 2005. Monazite and xenotime petrogenesis in the contact aureole of the Makhavinekh Lake Pluton, northern Labrador. Contributions to Mineralogy and Petrology 148 (5), 524–541.
Mohr, D.V., 1984. Zoned porphyroblasts of metamorphic monazite in the Anakeesta Formation, Great Smoky Mountain, North Carolina. American Mineralogist 69, 98–103.
Möller, A., O'Brien, P., Kennedy, A., Kröner, A., 2002. Polyphase zircon in ultrahigh-temperature granulites (Rogaland, SW Norway): constrains for Pb diffusion. Journal of Metamorphic Geology 20, 727–740.
Montel, J.-M., 1993. A model for monazite/melt equilibrium and application to the generation of granitic magmas. Chemical Geology 110 (1–3), 127–146.
Morel, M.L.A., Nebel, O., Nebel-Jacobsen, Y.J., Miller, J.S., Vroon, P.Z., 2008. Hafnium isotope characterization of the GJ-1 zircon reference material by solution and laser ablation MC-ICPMS. Chemical Geology 255 (1–2), 231–235.
Nagasawa, H., 1971. Partitioning of Eu and Sr between coexisting plagioclase and K-feldspar. Earth and Planetary Science Letters 13 (1), 139–144.
Nasdala, L., et al., 2003. Spectroscopic methods applied to zircon. Reviews in Mineralogy and Geochemistry 53, 428–467.
Ni, Y., Hughes, J., Marino, A., 1995. Crystal chemistry of the monazite and xenotime structure. American Mineralogist 80, 21–26.
Paces, J.B., Miller, J.D.J., 1993. Precise U–Pb ages of Duluth Complex and related mafic intrusions, northeastern Minnesota: geochronological insights to physical, petrogenetic, paleomagnetic, and tectonomagmatic processes associated with the 1.1 Ga Midcontinent Rift System. Journal of Geophysical Research 98, 13997–14013.
Paton, C., et al., 2010. Improved laser ablation U–Pb zircon geochronology through robust downhole fractionation correction. Geochemistry, Geophysics, Geosystems 11 (3), 2010.
Pedersen, R.B., Dunning, G.R., Robins, B., 1989. U–Pb ages of nepheline syenite pegmatites from the Seiland Magmatic Province, N. Norway. The Caledonide Geology of Scandinavia 3–5.
Poitrasson, F., Chenery, S., Bland, D.J., 1996. Contrasted monazite hydrothermal alteration mechanisms and their geochemical implications. Earth and Planetary Science Letters 145, 79–96.
Pyle, J.M., Baldwin, J.A., 2006. Temperature-time paths from phosphate accessory phase paragenesis in the Honey Brook Upland and associated cover sequence, SE Pennsylvania, USA. Lithos 88 (1–4), 201–232.
Pyle, J.M., Spear, F.S., 1999. Yttrium zoning in garnet: coupling of major and accessory phases during metamorphic reactions. Geological Materials Research 1, 1–49.
Pyle, J.M., Spear, F.S., 2003. Four generations of accessory-phase growth in low-pressure migmatites from SW New Hampshire. American Mineralogist 88, 338–351.
Pyle, J.M., Spear, F.S., Rudnick, R.L., McDonough, W.F., 2001. Monazite-xenotime and monazite–garnet equilibrium in a prograde pelite sequence. Journal of Petrology 42, 2083–2117.
Pyle, J.M., Spear, F.S., Cheney, J.T., Layne, G., 2005. Monazite ages in the Chesham Pond Nappe, SW New Hampshire, USA: implications for assembly of central New England thrust sheets. American Mineralogist 90, 592–606.
Root, D.B., Hacker, B.R., Mattinson, J.M., Wooden, J.L., 2004. Zircon geochronology and ca. 400 Ma exhumation of Norwegian ultrahigh pressure rocks; an ion microprobe and chemical abrasion study. Earth and Planetary Science Letters 228 (3–4), 325–341.
Root, D.B., et al., 2005. High-pressure allochthons overlie the ultrahigh-pressure Western Gneiss Region, Norway. Journal of Metamorphic Geology 23, 45–61.
Rubatto, D., 2002. Zircon trace element geochemistry: partitioning with garnet and the link between U–Pb ages and metamorphism. Chemical Geology 184, 123–138.
Rubatto, D., Gebauer, D., Compagnoni, R., 1999. Dating of eclogite-facies zircons: the age of Alpine metamorphism in the Sesia–Lanzo Zone (Western Alps). Earth and Planetary Science Letters 167, 141–158.
Rubatto, D., et al., 2000. Use of Cathodoluminescence for U–Pb Zircon Dating by Ion Microprobe; Some Examples from the Western Alps.
Rubatto, D., Hermann, J., Buick, I.S., 2006. Temperature and bulk composition control on the growth of monazite and zircon during low-pressure anatexis (Mount Stafford, central Australia). Journal of Petrology 47 (10), 1973–1996.
Rubatto, D., Hermann, J., Berger, A., Engi, M., 2009. Protracted fluid-induced melting during Barrovian metamorphism in the Central Alps. Contributions to Mineral and Petrology 158, 703–722.
Schaltegger, U., et al., 1999. Growth, annealing and recrystallization of zircon and preservation of monazite in high-grade metamorphism: conventional and in situ U–Pb isotope, cathodoluminescence and microchemical evidence. Contributions to Mineral and Petrology 134, 186–201.
Shakel, D.W., Silver, L.T., Damon, P.E., 1977. Observations of the history of the gneissic core complex, Santa Catalina Mtns., southern Arizona. Abstracts with Programs — Geological Society of America 9 (7), 1169–1170.
Simpson, R.L., Parrish, R.R., Searle, M., Waters, D., 2000. Two episodes of monazite recrystallization during metamorphism and crustal melting in the Everest region of the Nepalese Himalaya. Geology 28, 403–406.
Slama, J., et al., 2008. Plesovice zircon; a new natural reference material for U/Pb and Hf isotopic microanalysis. Chemical Geology 249 (1–2), 1–35.
Smith, H.A., Barreiro, B., 1990. Monazite U–Pb dating of staurolite grade metamorphism in pelitic schists. Contributions to Mineralogy and Petrology 105, 602–615.
Spear, F.S., Pyle, J.M., 2010. Theoretical modeling of monazite growth in a low Ca metapelite. Chemical Geology 273 (1–2), 111–119.
Spear, F.S., Cheney, J.T., Pyle, J.M., Harrison, T.M., Layne, G., 2008. Monazite geochronology in central New England; evidence for a fundamental terrane boundary. Journal of Metamorphic Geology 26 (3), 317–329.
Speer, J.A., 1982. Zircon. Reviews in Mineralogy 5, 67–112.
Terry, M.P., Robinson, P., Hamilton, M.A., Jercinovic, M.J., 2000. Monazite geochronology of UHP and HP metamorphism, deformation, and exhumation, Nordøyane, Western Gneiss Region, Norway. American Mineralogist 85, 1651–1664.
Timms, N.E., et al., 2010. Relationship among titanium, rare earth elements, U/Pb ages and deformation microstructures in zircon; implications for Ti-in-zircon thermometry. Chemical Geology 280 (1–2), 33–46.
Tomascak, P.B., Krogstad, E.J., Walker, R.J., 1996. U–Pb monazite geochronology of granitic rocks from Maine; implications for late Paleozoic tectonics in the Northern Appalachians. Journal of Geology 104 (2), 185–195.
Tomkins, H.S., Pattison, D.R.M., 2007. Accessory phase petrogenesis in relation to major phase assemblages in pelites from the Nelson contact aureole, southern British Columbia. Journal of Metamorphic Geology 25 (4), 401–421.

Tucker, R.D., et al., 2004. Thrusting and extension in the Scandian hinterland, Norway: new U–Pb ages and tectonostratigraphic evidence. American Journal of Science 304, 477–532.
Uher, P., Černý, P., 1998. Zircon in Hercynian granitic pegmatites of the Western Carpathians, Slovakia. Geologica Carpathica (Bratislava) 49 (4), 261–270.
Vavra, G., 1990. On the kinematics of zircon growth and its petrogenetic significance; a cathodoluminescence study. Contributions to Mineralogy and Petrology 106 (1), 90–99.
Ventura, G.D., et al., 1996. Monazite–huttonite solid-solutions from the Vico Volcanic Complex, Latium, Italy. Mineralogical Magazine 60, 751–758.
Walsh, E.O., Hacker, B.R., 2004. The fate of subducted continental margins: two-stage exhumation of the high-pressure to ultrahigh-pressure Western Gneiss complex, Norway. Journal of Metamorphic Geology 22, 671–689.
Wark, D.A., Miller, C.F., 1993. Accessory mineral behavior during differentiation of a granite suite: monazite, xenotime and zircon in the Sweetwater Wash Pluton, southeastern California, U.S.A. Chemical Geology 110 (1–3), 49–67.
Watson, E.B., Harrison, T.M., 2005. Zircon thermometer reveals minimum melting conditions on earliest Earth. Science 308, 841–844.
Watson, E.B., Wark, D.A., Thomas, J.B., 2006. Crystallization thermometers for zircon and rutile. Contributions to Mineralogy and Petrology 151, 413–433.
Wiedenbeck, M., et al., 1995. Three natural zircon standards for U–Th–Pb, Lu–Hf, trace element and REE analyses. Geostandards Newsletter 19 (1), 1–23.
Williams, M.L., Jercinovic, M.J., Terry, M.P., 2002. Microprobe monazite geochronology: putting absolute time into microstructural analysis. Journal of Structural Geology 24, 1013–1028.
Williams, M.L., Jercinovic, M.J., Hetherington, C.J., 2007. Microprobe monazite geochronology: understanding geologic processes by integrating composition and chronology. Annual Review of Earth and Planetary Sciences 35, 137–175.
Wing, B.A., Ferry, J.M., Harrison, T.M., 2003. Prograde destruction and formation of monazite and allanite during contact and regional metamorphism in pelites: petrology and geochronology. Contributions to Mineralogy and Petrology 145, 228–250.
Wolf, M.B., London, D., 1995. Incongruent dissolution of REE- and Sr-rich apatite in peraluminous granitic liquids: differential apatite, monazite, and xenotime solubilities during anatexis. American Mineralogist 80, 765–775.
Woodhead, J.D., Hergt, J.M., 2005. A preliminary appraisal of seven natural zircon reference materials for in situ Hf isotope determination. Geostandards and Geoanalytical Research 29 (2), 183–195.
Woodhead, J.D., Hellstrom, J.C., Hergt, J.M., Greig, A., Maas, R., 2007. Isotopic and elemental imaging of geological materials by laser ablation inductively coupled plasma mass spectrometry. Journal of Geostandards and Geoanalytical Research 31, 331–343.
Xie, L., Zhang, Y.-B., Zhang, H., Sun, J., Wu, F.-Y., 2008. In situ simultaneous determination of trace elements, U–Pb and Lu–Hf isotopes in zircon and baddeleyite. Chinese Science Bulletin 53 (10), 1565–1573.
Yang, P., Pattison, D., Baldwin, J.A., 2006. Genesis of monazite and Y zoning in garnet from the Black Hills, South Dakota. Lithos 88 (1–4), 233–253.
Young, D.J., et al., 2007. Amphibolite to ultrahigh-pressure transition in western Norway: implications for exhumation tectonics. Tectonics 26, TC1007. http://dx.doi.org/10.1029/2004TC001781.
Yuan, H.-L., et al., 2008. Simultaneous determinations of U/Pb age, Hf isotopes and trace element compositions of zircon by excimer laser ablation quadrupole and multiple collector ICP-MS. Chemical Geology 247 (1–2), 100–118.
Zhu, X.K., O'Nions, R.K., 1999a. Monazite chemical composition: some implications for monazite geochronology. Contributions to Mineralogy and Petrology 137, 351–363.
Zhu, X.K., O'Nions, R.K., 1999b. Zonation of monazite in metamorphic rocks and its implications for high-temperature thermochronology: a case study from the Lewisian terrain. Earth and Planetary Science Letters 171, 209–220.
Zhu, X.K., O'Nions, R.K., Belshaw, N.S., Gibb, A.J., 1997. Significance of in situ SIMS chronometry of zoned monazite from the Lewisian granulites, Northwest Scotland. Chemical Geology 135 (1–2), 35–53.